Supercond. Sci. Technol. **34** (2021) 035026 (15pp) https://doi.org/10.1088/1361-6668/abdc7f

SMART conductor on round core (CORC®) wire via integrated optical fibers

F Scurti[1], J D Weiss[2,3], D C van der Laan[2,3] and J Schwartz[1]

[1] Department of Engineering Science and Mechanics, The Pennsylvania State University, University Park, PA 16802, United States of America
[2] Advanced Conductor Technologies LLC, Boulder, CO 80301, United States of America
[3] Department of Physics, the University of Colorado, Boulder, CO 80309, United States of America

E-mail: fscurti@psu.edu

Received 25 November 2020
Accepted for publication 17 January 2021
Published 4 February 2021

Abstract

Superconducting cables based on high temperature superconductors (HTS) are necessary for applications requiring large currents and low inductance, such as compact fusion reactors. In this paper, we report the proof-of-concept of a SMART Conductor on Round Core (CORC®) wire realized via integration of optical fibers into the copper core. A SMART CORC® wire with integrated optical fibers was manufactured and its capabilities have been experimentally demonstrated. Results show that by interrogating the optical fibers via Rayleigh backscattering, a Spectral Shift signal as a function of time and position along the cable can be used to detect and locate hot-spots that are developed within the wire or its terminations. It has been found that highly localized current injection into the terminations could initiate hot-spots within the cable at locations where current redistribution between tapes occur. This effect is virtually eliminated when adequate current connections are used that inject current evenly along the cable terminations. Normal zone propagation velocities have been calculated as a function of time using Spectral Shift data for a heater-induced quench as well as a quench induced by overcurrent. In both cases the normal zone propagation velocity was about 6 cm s^{-1}, but in the heater-induced experiment it was preceded by 500 ms of slower propagation at 2.5 cm s^{-1}.

Keywords: optical fiber sensors, quench detection, distributed sensing, Rayleigh scattering, CORC® wire, high temperature superconductors

(Some figures may appear in colour only in the online journal)

1. Introduction

Since their discovery, high temperature superconductors (HTS) caused a strong interest in the scientific community, mostly because of their high critical temperature and large current densities at high background fields. A few HTS materials have evolved beyond the R&D phase, becoming a viable conductor option for magnets. A leading option for magnets is (RE)$Ba_2Cu_3O_{7-x}$ (REBCO) conductors [1–7]. In addition to conductor development, the last decade has seen a rapid advancement in cable technology, especially based on REBCO [3, 8–15]. Although some magnets can be successfully wound from a single REBCO conductor [4, 16], like high field inserts for users magnets or superconducting motors and generators. The high aspect ratio and in-field performance anisotropy of REBCO tapes causes challenges in the design of high-field magnets. Other issues related to using a single conductor are high magnet inductance, which requires relatively slow charging and discharging, and potential issues at local tape defects that may cause a hotspot and potentially conductor burnout. Many applications need to be ramped at relatively high rates and thus require a low inductance. The high operating current cannot be achieved with a single tape and require many tapes to be bundled into a

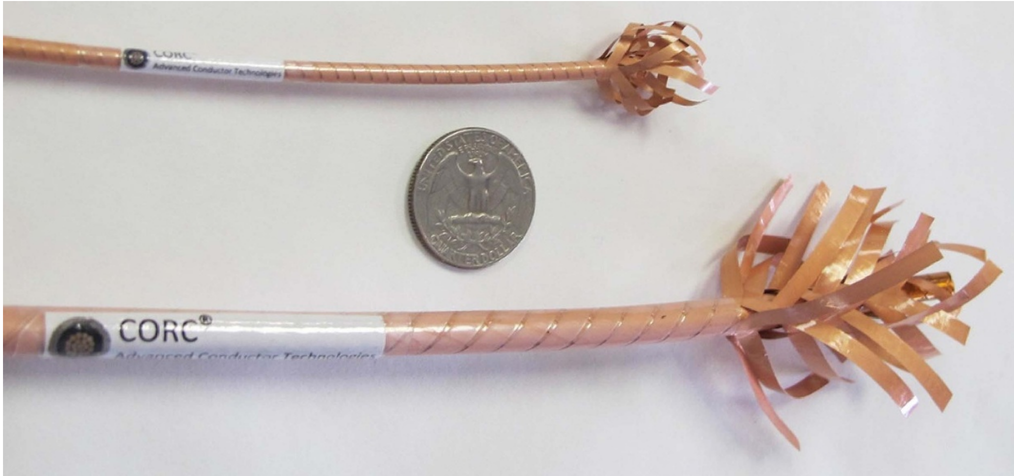

Figure 1. Image of conventional CORC cable and wire samples.

cable [8, 17–19]. One of the most promising REBCO cable technologies is the Conductor on Round Core (CORC®). An image of CORC® cables and wires can be seen in figure 1. Other cable technologies that use REBCO conductors are the Roebel [11, 12, 20] and twisted-stacked designs [9, 21, 22]. Advantages of CORC® cables, when compared to Roebel and twisted-stacked approaches, include superior flexibility and isotropic in-field performance [13, 15, 23–26]. Bundling several tapes in parallel provides current with the ability to bypass tape effects, potentially allowing for safer magnet operation. Several magnets wound from CORC® cables or wires have been successfully demonstrated and allowed operation to within the flux-flow regime without causing a quench [27–29].

Reliable and accurate quench detection is especially challenging in magnets wound from single HTS tapes where the normal zone propagation velocity (NZPV) is several orders in magnitude lower than in LTS [30–37] . Current sharing between tapes in HTS cables such as CORC® may significantly ease the quench detection challenge in HTS magnets, as long as transition into the dissipative state is detected in time. Knowledge of the operating status such as local temperature and strain state along the length of the magnet cable would be highly beneficial for the reliable operation of large magnet systems. Such information would allow detection of local hotspots that may eventually develop into a magnet quench. One potential method to obtain real-time information about the local operating state of HTS cables is with integrated Rayleigh-scattering interrogated optical fibers (RIOF). The temperature and strain state is determined on a millimeter length scale from the spectral shift in the reflected light caused by the alteration of the spatial distribution of defects in the fiber, as explained in [38, 39]. In prior work, the RIOF technique has been demonstrated within HTS coils by co-winding optical fibers with conductor [40, 41] and by embedding optical fibers into the architecture of a REBCO conductor, yielding a 'SMART REBCO Conductor' [42]. In these embodiments, the RIOF technique proved to be more sensitive to normal zones than voltage, both temporally and spatially. In particular, the temperature sensitivity of RIOF can be appreciated by looking at the results previously reported in [42] as figure 11. These show that the embedded optical fiber (in that embodiment embedded into AMSC's REBCO wire) is more sensitive to a temperature increase than a thermocouple, with a sensitivity of about 4 GHz K^{-1} in the range 82–86 K. Additionally, further prior work showed that cryogenic thermal sensitivity and response time of optical fibers interrogated by Rayleigh backscattering can be enhanced by dedicated fiber coatings, at temperatures as low as 4.2 K [43].

Earlier work performed on a CORC® wire containing integrated optical fibers focused on measurement of strain as a function of position along a bent cable, at bending radii from 10 cm to 6 cm, as well as the response time of the optical fiber to the onset of a quench, compared to that of conventional voltage wire measurements [44]. This paper focuses on all the capabilities that embedded optical fibers provide by measuring a signal, the spectral shift, that is proportional to the local temperature along the conductor length and within its terminations during normal operation and when the conductor is driven into the dissipative state. Such dissipative state is induced by operating the CORC® wire at currents exceeding the critical current (I_c), or when a hotspot is introduced via a localized heat input.

2. Experimental approach

2.1. Optical fiber integration

Commercial off the shelf single-mode telecommunication-grade optical fibers have been integrated into the copper core of a CORC® wire by Advanced Conductor Technologies before winding the REBCO conductors. The copper core contained three extruded grooves that allowed easy insertion of the optical fibers, while also allow twisting of the core to introduce a twist pitch of 38 mm. The embedded optical fibers have a cladding of 125 μm in diameter and comprise an acrylate coating. A photograph of the copper core with integrated fibers is shown in figure 2(a). Note that optical fiber integration into the CORC® wire was driven by the following requirements:

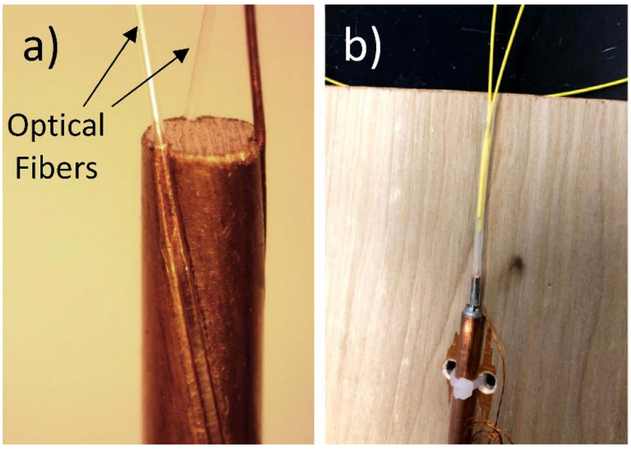

Figure 2. (a) Optical image of copper core with two integrated optical fibers and a copper wire; (b) close-up photo of optical fibers exiting SMART CORC® wire.

Table 1. Summary of conductor and SMART CORC® wire specifications.

	Item	Value	Unit
REBCO Conductors	Conductor width	2	mm
	Substrate thickness	30	μm
	Total Cu stabilizer thickness	10	μm
	Average I_c (77 K)	56	A
SMART CORC® Wire	Cu core diameter	2.6	mm
	Polyester insulation thickness	30	μm
	Cable outer diameter	3	mm
	Nominal cable I_c (77 K)	448	A
	Termination length	10	cm
	Cable region length	24	cm
	Total cable length	46	cm

the optical fibers fit into the cable architecture without major changes to commercial CORC® cables, optical fibers do not alter electrical and mechanical performance of conventional CORC® cables, the manufacturing of SMART cable is scalable to long length. A total of 8 SuperPower REBCO tapes of 2 mm width were wound in four layers onto the copper core. A 30 μm thick polyester heat shrink tube was applied to the outside of the CORC® wire to hold the tapes in place and to provide electrical insulation. Terminations consisting of a copper tube filled with indium solder were applied to the CORC® wire in which the optical fibers extended through the solder, providing easy access to interrogate the fibers, while also allowing temperature measurements within the terminations. A photo of the termination and optical fibers exiting the core can be seen in figure 2(b). More information about the conductor specifications is included in table 1. A schematic drawing of the mutual positions of the wire region, current adapters and optical fibers is shown in figure 5.

2.2. Quench experiments

The purpose of these experiments is to evaluate the detection capabilities of SMART CORC® wires to different types of perturbations and normal zone initiation modes. A photograph of the experimental setup used for these experiments is shown in figure 3. The sample is connected to the power supply via current adapters clamped onto the sample terminations. Both sample and terminations are anchored to a wooden board, and all together are submerged in a liquid nitrogen bath. Two different sets of current adapters have been used. Adapters covering full length of the CORC® terminations (figures 3(b) and (c)) are made of high purity, oxygen-free copper, whereas shorter, aluminum adapters that only cover about halve the termination inject current only locally into the CORC® terminations (figures 3(a) and (d)).

The SMART CORC® wire is instrumented with voltage taps and a nickel-chromium wire wound around the sample, on top of the polyester insulation, to act as a spot heater to create the thermal perturbation that is needed to initiate a normal zone. The heater wire is partly insulated from the liquid nitrogen bath by Kapton tape. Two different experimental procedures have been used to drive the sample into the dissipative regime. The first procedure involves a transport current that is increased from zero to a set-point value, and then held constant over a time interval (plateau), until it is ramped back to zero. We will refer to this type of experiment as ‘overcurrent’, although the target current may or may not be above the critical current of the sample (I_c). The second procedure is analogous to the former, with the addition of the heater firing during the current plateau to cause a thermal runaway that ultimately would lead to a quench. This type of experiment will be referred to as ‘quench’. Figure 4 outlines the time evolution of current and heater signals as they would evolve during the two types of experiments. In both cases, the voltage is measured by voltage taps connected to Digital Multimeters, while the optical fibers that are embedded in the terminations and CORC® wire is interrogated via Rayleigh backscattering. This leads to a Spectral Shift signal acquired as a function of position along the sample length and time. All signals are synchronized in time because they are acquired against the same clock with a dedicated LabVIEW application. The spatial resolution was 2.61 mm and the temporal resolution was about 20 ms. It is worth noting that although the optical fiber is sensitive to both strain and temperature changes, in this work the SMART CORC® wire is not subject to mechanical perturbations or external magnetic field; for these reasons, the spectral shift signal is expected to be only affected by temperature changes. Conversely, when the SMART CORC® is only perturbed mechanically, as it is the case in the bending experiments reported in section 3.2 of [44], the spectral shift simply scales with strain.

3. Results and discussion

3.1. Quench experiments performed using small current adapters

The two optical fibers have been tested for integrity and functionality at room temperature after being embedded into the CORC® wire. The optical tests have been repeated after cooling the sample to 77 K and indicate that the cool-down

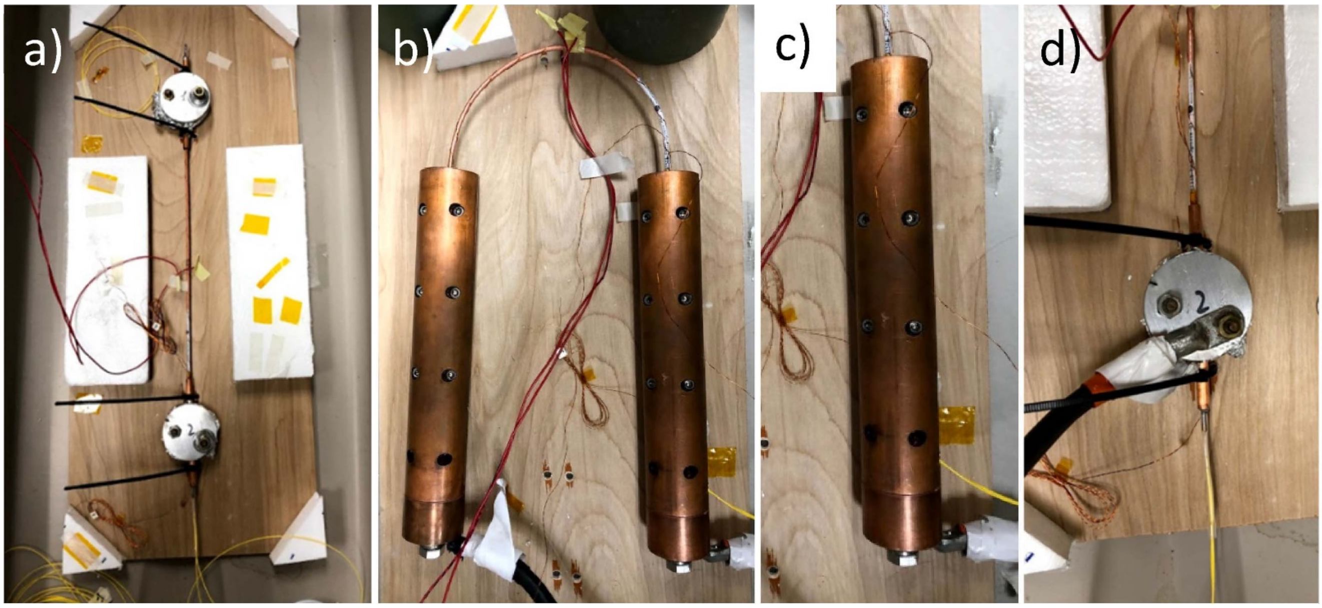

Figure 3. Photos of: (a) experimental setup with straight SMART CORC® wire; (b) experimental setup with wire bent to 55 mm radius; (c) large, copper current adapter; (d) small, aluminum current adapter.

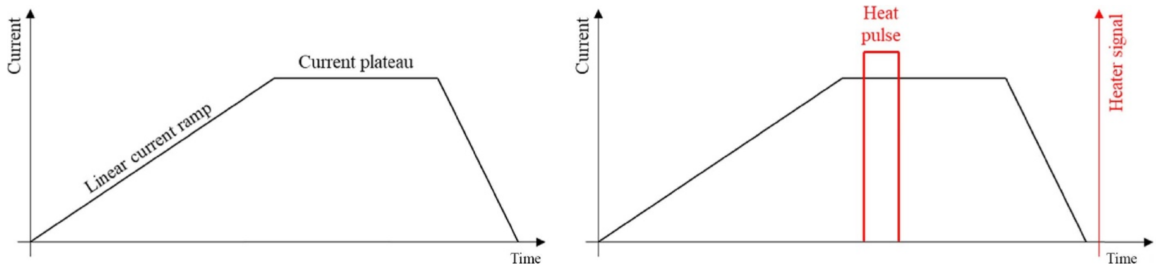

Figure 4. Schematic plots of transport current and heater signal time evolution for overcurrent (left) and quench (right) procedures.

did not affect the fiber integrity or functionality. The critical current at an electric field criterion of 1 μV cm^{-1} was 340 A at 77 K in self-field. Since the fibers have survived the integration and CORC® wire manufacturing process unaffected, the fiber integration method is considered successful.

The results of a quench experiment are shown in figures 5–8. The small current adapters were used in this experiment because they have shown significant Joule heating [44]. For this experiment, the current was increased linearly at 10 A s^{-1} before it was kept constant at 430 A, which is 125% of I_c; a heat pulse was released by the external heater during the current plateau, having a gross power of 16 W for 2 s. The Spectral Shift map for this experiment is shown in figure 5, along with a schematic drawing illustrating the cable and current adapters with approximate locations on the position axis. Additionally, the time profile of the transport current is shown next to the Spectral Shift map. The locations where current is injected into the terminals are undergoing Joule heating, as evidenced by the increasing Spectral Shift. In addition to the current termination regions, the Spectral Shift clearly shows that a normal zone is initiated by the heater and spreads throughout the cable sample. The heater is located at 0.2 m on the position axis. Note that in this case the color bar is limited to 30 GHz to enhance the color contrast; this does not mean that 30 GHz is the maximum Spectral Shift measured throughout the experiment, but only that Spectral Shift values of 30 GHz or greater are shown in dark red.

From the plot in figure 5 it is also possible to appreciate that the normal zone development is not symmetric. Some regions generate more Spectral Shift than others, and the time to recovery also differs for different regions. On the left of the normal zone initiation spot, the Spectral Shift appears stronger and recovers more slowly after the current is brought to zero. Moreover, even within this left region, or within the right region from the heater, the Spectral Shift spatial distribution is not uniform.

A more detailed view of these results is shown in figure 6, where the Spectral Shift is presented as a function of position, at different times before, during and after the heat pulse is applied. The inset shows transport current and heat pulse as a function of time during the same experiment. The Spectral Shift and thus temperature in the regions of the current adapters (0–0.05 m and 0.35–0.4 m) is constant during the time 45–49 s, consistent with the transport current being constant in this time period. The initiation by the heater is also clearly seen, centered at 0.2 m. The time evolution of the different

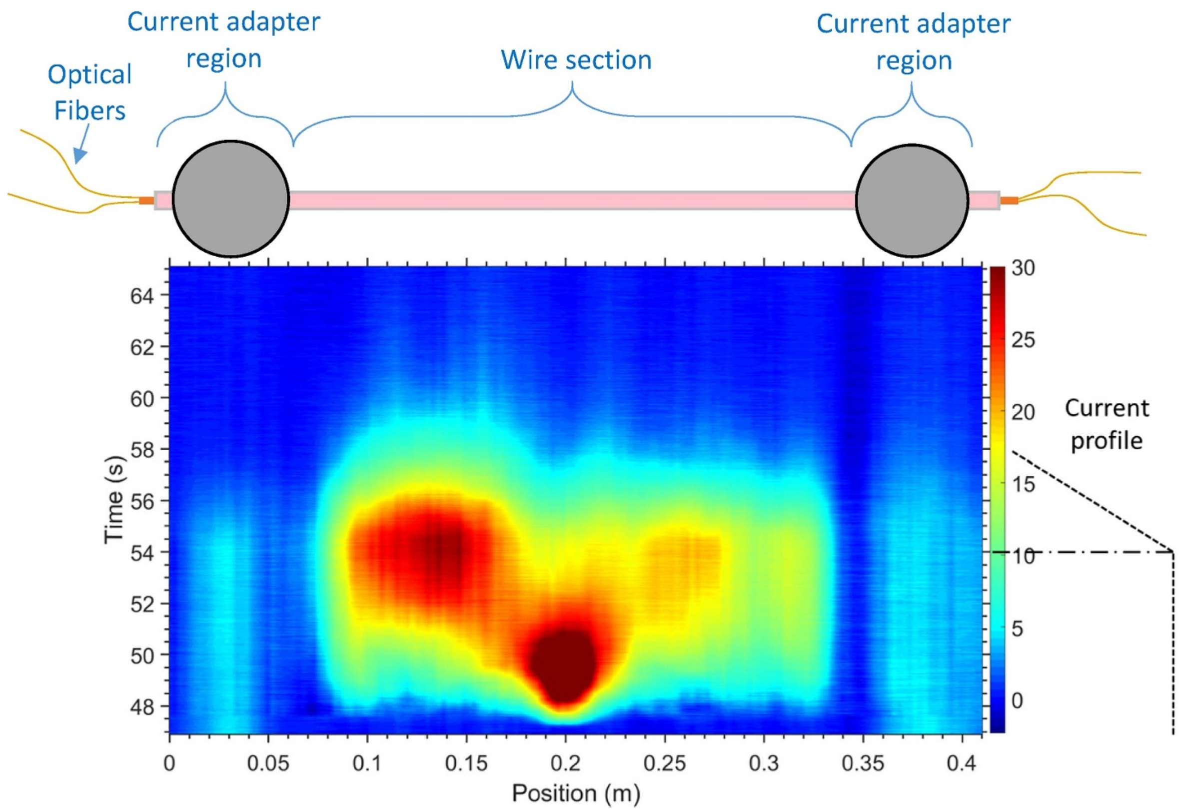

Figure 5. Spectral Shift map highlighting the time interval after quench initiation.

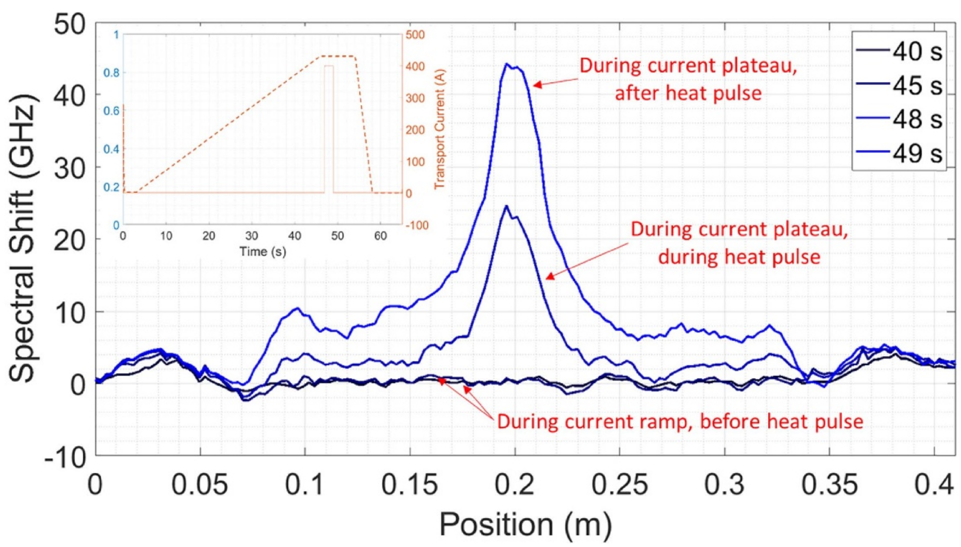

Figure 6. Evolution of Spectral Shift spatial profiles during the instability.

signals is better seen in figure 7, where the Spectral Shift is plotted as a function of time at three positions: within the region of the left current adapter (0.033 m), at the center of the heater region (0.2 m), and within the region of the right current adapter (0.373 m). Along with the Spectral Shift, the plot includes the transport current and heater signals. Note that the transport current is the actual current flowing into the cable, measured with a shunt resistor, and is plotted to scale, whereas the heater signal, although it is also a measured signal, is not to scale. The Spectral Shifts at locations 0.033 m and 0.373 m follow the time profile of the transport current closely, consistent with a temperature increase caused by Joule heating at the resistive connections. The temperature increase levels off when the current is constant and the temperature decreases slowly when the current is brought to zero. A slower decay than the current signal is an additional confirmation of the nature of the signal; when the source is turned off (transport current in this case) the temperature (Spectral Shift) will decay

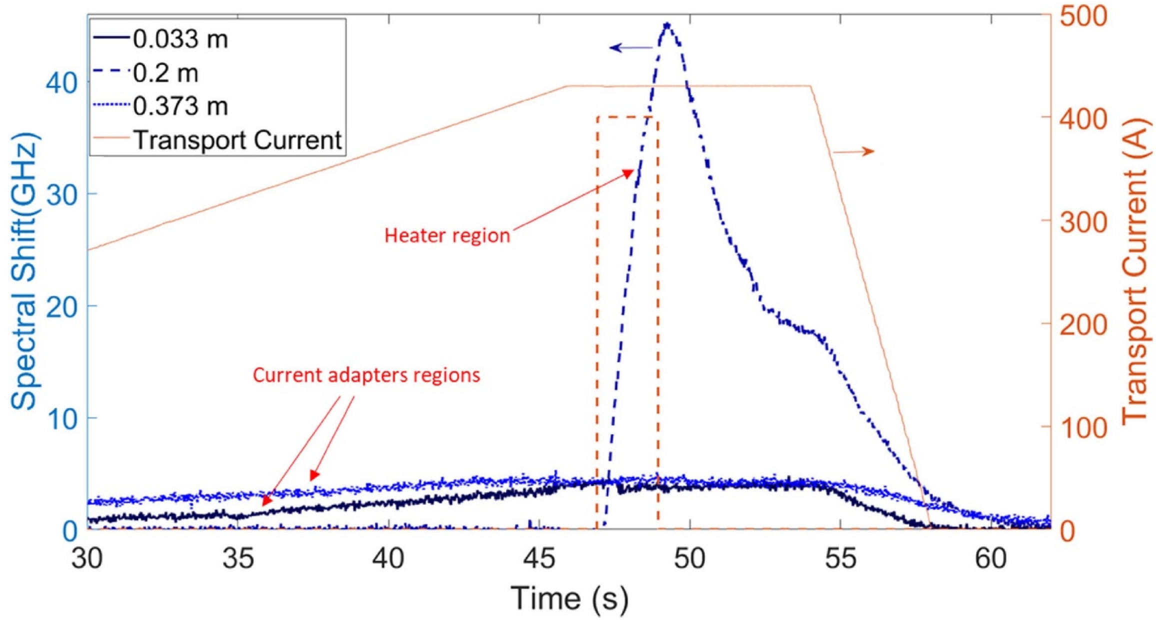

Figure 7. Time evolution of Spectral Shift throughout the experiment, at different locations including current adapters and heater regions, along with transport current and heater signals.

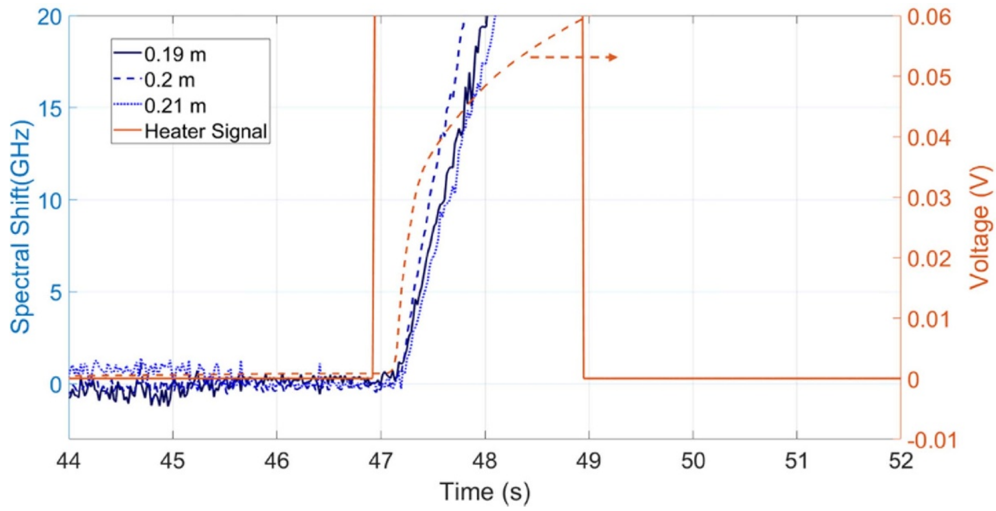

Figure 8. Comparison of the functions of time of signals from end-to-end voltage tap (right axis) and optical fiber (left axis).

gradually because of the time constant for heat transfer away from the source.

Another interesting aspect highlighted by these results can be seen in figure 7. The Spectral Shift measured at the heater location tends to level off towards the end of the current plateau, indicating a local equilibrium is being attained between heat source and cooling; however, as soon as the transport current is reduced, beginning at $t = 54$ s, the slope of the Spectral Shift versus time increases again. The comparison with the voltage signal measured by the end-to-end voltage tap is shown, on a shorter time scale, in figure 8. From the data in figure 5 it can be noted that the two regions between the central cable section and each current adapter (approximately 0.05–0.07 m and 0.34–0.36 m) experience no increase in temperature and show almost no variation in Spectral Shift. This is due to the increased copper cross-section of the terminations that prevents further propagation of the normal zone.

3.2. Quench experiments performed using two different current adapters

Another set of experiments has been carried out using a slightly different setup: a straight cable sample equipped with two different current adapters. The small, aluminum adapter was used to inject current into the left termination whereas the larger, cylindrical copper adapter was used to inject current into the termination on the right side of the sample. In this setup, the right current connection offers a lower overall resistance than the one on the left. Also, due to a larger contact area, it can be assumed that all REBCO tapes within

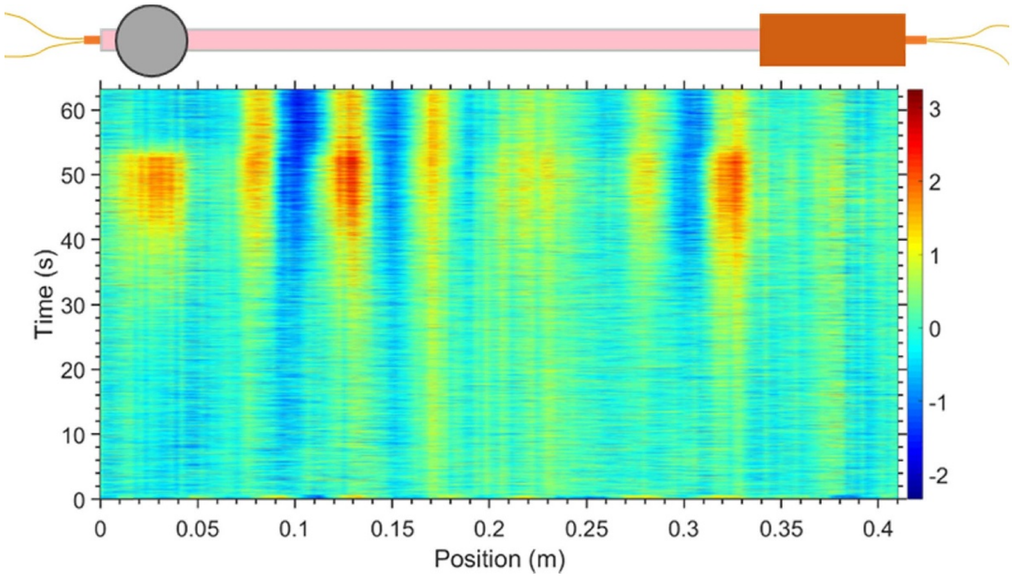

Figure 9. Temporal and spatial evolution of Spectral Shift throughout the current ramp up; hot spots are still generated but at different locations compared with the set-up comprising Al connections at both cable ends. The sketch atop the graph illustrates the current adapters used in this experiment.

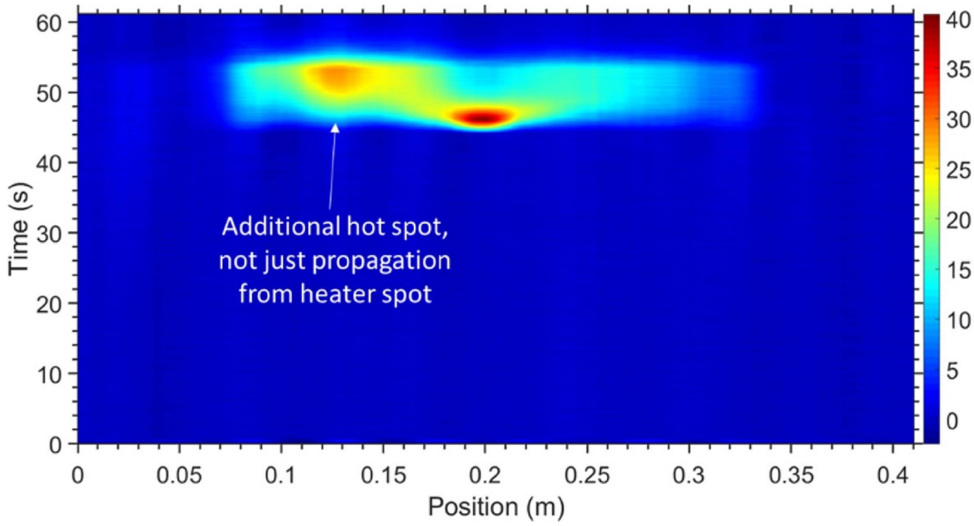

Figure 10. Spectral shift map of a quench experiment with the mixed current adapters approach.

the CORC® wire termination are interfacing with the copper current adapter with an equivalent resistive path, whereas this is not the case when using the smaller aluminum adapter. A schematic illustration of this approach is included as a sketch as part of figure 9.

The first experiment with the new connections setup is of the type 'overcurrent', so no heat is introduced with the heater and the transport current is linearly increased up to a plateau of 430 A, or 125% of I_c, and then quickly brought to zero. Results of this experiment are shown, in the form of a Spectral Shift map, in figure 9. It can be clearly noticed that the Spectral Shift increase in the left terminal where the small current adapter is used is still present, although reduced in magnitude compared to the previous setup when small current adapters were used at both terminations. The right current termination no longer shows an increase in Spectral Shift, indicating that the temperature of the termination remains constant.

A quench experiment similar to the one performed with the two small current adapters has been carried out with this second setup, where current is increased at 10 A s^{-1} and held constant at 430 A, or 125% of I_c, at which time the heater was activated at 16 W for 2 s. The results of this experiment are shown as a Spectral Shift map in figure 10. Note that the normal zone is indeed initiated at the heater location, and that the second location where a higher increase in temperature is measured (around 0.125 m) remained. The second hotspot is seen even more clearly from plots of Spectral Shift versus time at 0.125 m and 0.2 m as well as Spectral Shift versus position at several time intervals before and during the transient. These plots are shown in figures 11 and 12.

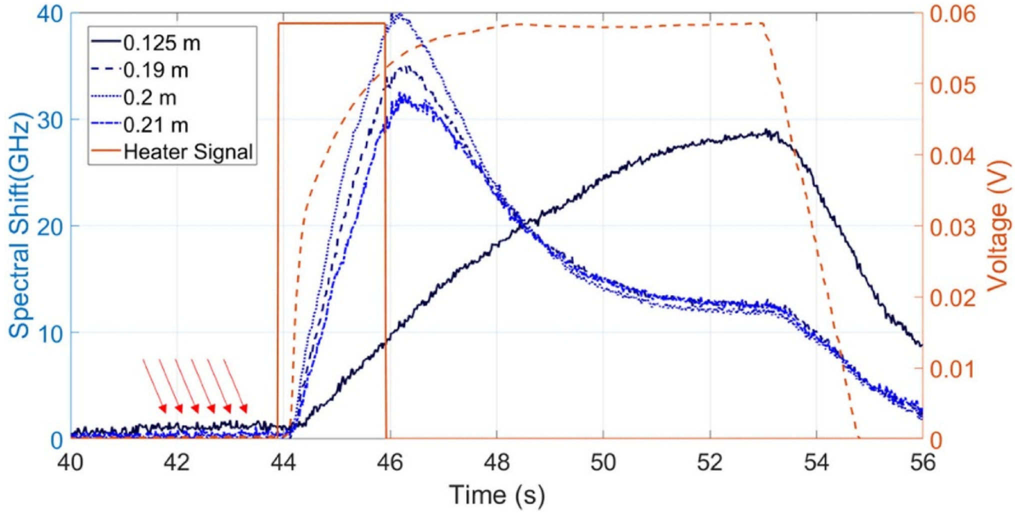

Figure 11. Spectral shift, voltage and heater signal as a function of time from the quench experiment when two types of current adapters are used.

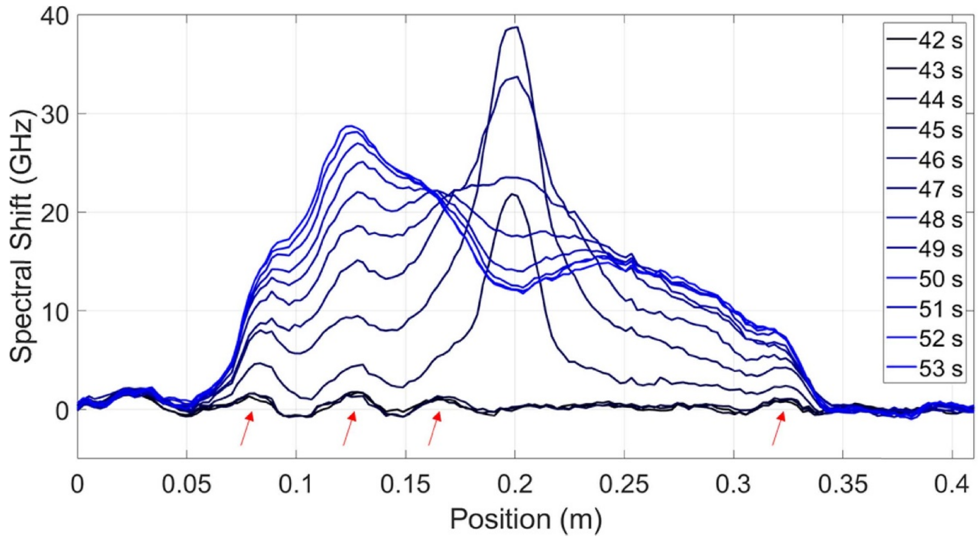

Figure 12. Time evolution of spatial profile of Spectral Shift spanning times before, during, and after the heat pulse. Note the locations with prior hot-spots that are enhanced and grow following the heat pulse (marked with red arrows). The heat input during this run is 16 W for 2 s.

The Spectral Shift at location 0.125 m, which is where the 'secondary' hot-spot appears, starts to increase noticeably a few seconds after the Spectral Shift at the heater region increased (locations 0.19 m, 0.20 m, and 0.21 m, also shown on the same graph). Although the Spectral Shift at location 0.125 m, which is where the secondary hot-spot appears, starts to increase approximately at the same time as the heater location (0.19–0.21 m), the two locations have very different time evolutions, indicating that the secondary hot spot is not simply related to the heater spot via heat transfer, but they are sustained by different heat sources. Also, location 0.125 m shows a small but noticeable increase in Spectral Shift prior to the heat pulse. The potential mechanism causing the secondary hotspot could be related to the small current adapter used to inject current into the terminal on the left. The adapter is only in close contact with a limited number of tapes in the CORC® wire, forcing the current to redistribute between tapes along the cable. It is therefore highly likely that some of the tapes carry a much higher share of the current than others, therefore operating close to their I_c. Any increase in temperature would force these tapes into their dissipative state, causing them to increase in temperature, which his than measured by the fiber. The plots in figure 12 show that after the heat pulse ends, the location along the sample with the highest temperature, being the most likely to fail, is the secondary hotspot located at 0.125 m, not the spot where the heater is attached. In other words, if an external perturbation hits the cable (here simulated with the heat pulse), the regions that are most affected can be different from the location where the perturbation hits. These results suggest that these locations that generate hot-spots depend not only on the cable itself (i.e. I_c of single wires, manufacturing history of the particular batch, current

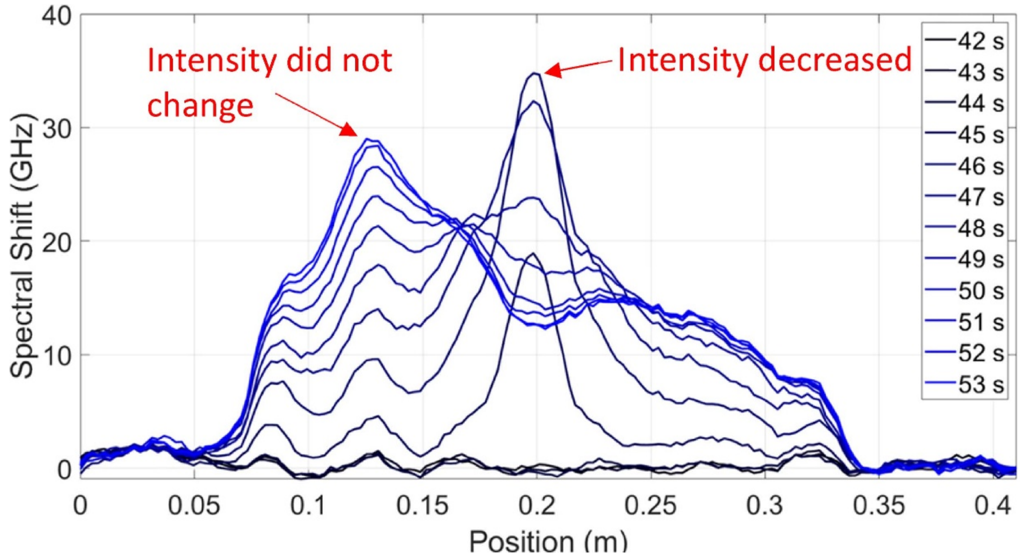

Figure 13. Time evolution of spatial profile of Spectral Shift spanning times before, during, and after the heat pulse. Only difference from the experiment that produced the results in figure 12 is a lower heat input of 14 W for 2 s during this run. *Note that the Spectral Shift intensity at 0.125 m is exactly the same as the previous case with higher heat input.*

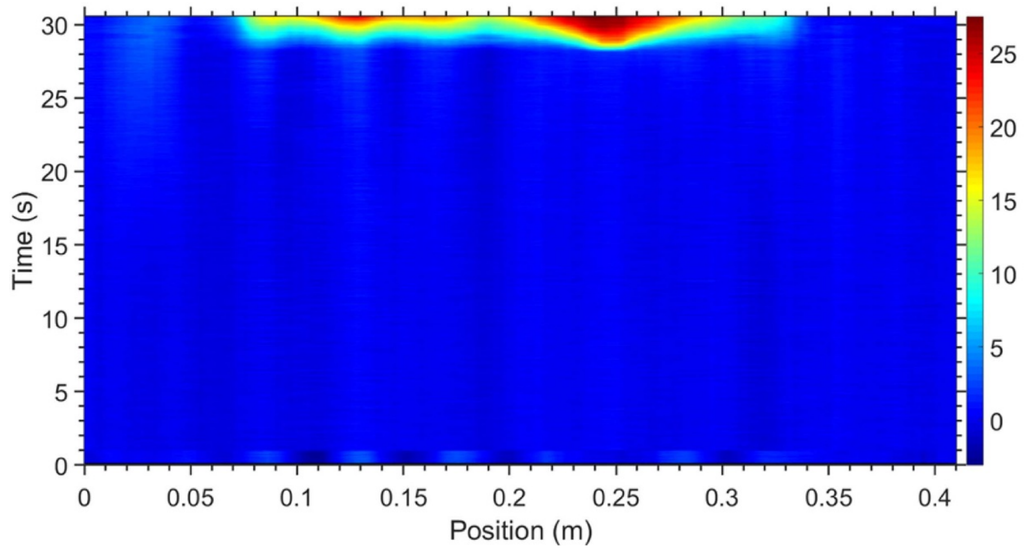

Figure 14. Spectral Shift map of overcurrent experiment when two types of current adapters are used. Current is increased to 520 A, or 150% of I_c.

connections, etc.), but also on the current distribution between tapes in the sample.

The experiment was repeated using a reduced heater power of 14 W instead of 16 W. The results are analogous to those obtained with the higher heater power, confirming the repeatability of the results. Furthermore, by comparing the results of these two runs that differ only in heater power, another important phenomenon is noticed: although the resulting response of the sample is similar and the peak Spectral Shift at the heater spot (0.2 m) scales with the heater power (decreasing from 38.76 GHz to 34.78 GHz), the maximum Spectral Shift measured at the strongest secondary hotspot, centered at 0.125 m, is independent of the heater power (figure 13). This suggests that the secondary hot-spot is due to the inability to effectively redistribute current between tapes, caused by the inadequate current adapter, and that the heat input only forces the current to redistribute.

An 'overcurrent' experiment is carried out with a current plateau at 520 A, or 150% of I_c; results are seen in figure 14. The quench initiation spot is no longer the heater spot, as expected, but is located at about 0.25 m, which is also different from the location of the secondary hotspot defined previously. To understand how the spatial distribution of the Spectral Shift evolves with time, and how different spots initiate and evolve temporally, the Spectral Shift at locations 0.13 m, 0.24 m and 0.25 m are plotted as a function of time in figure 15, along with current and voltage signals. The Spectral Shift at location 0.13 m shows a slight but clear increase

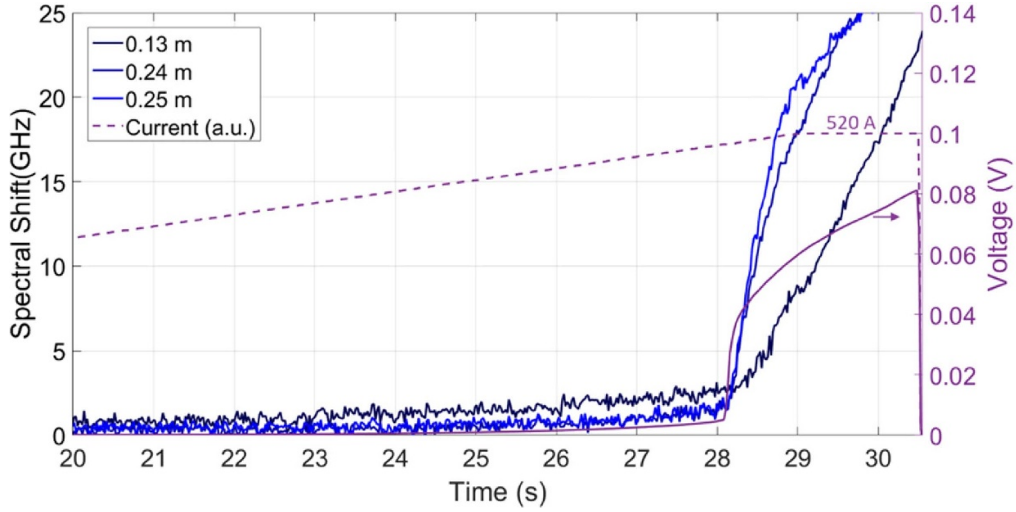

Figure 15. Time evolution of Spectral Shift throughout the experiment, at different locations, along with transport current and voltage signals.

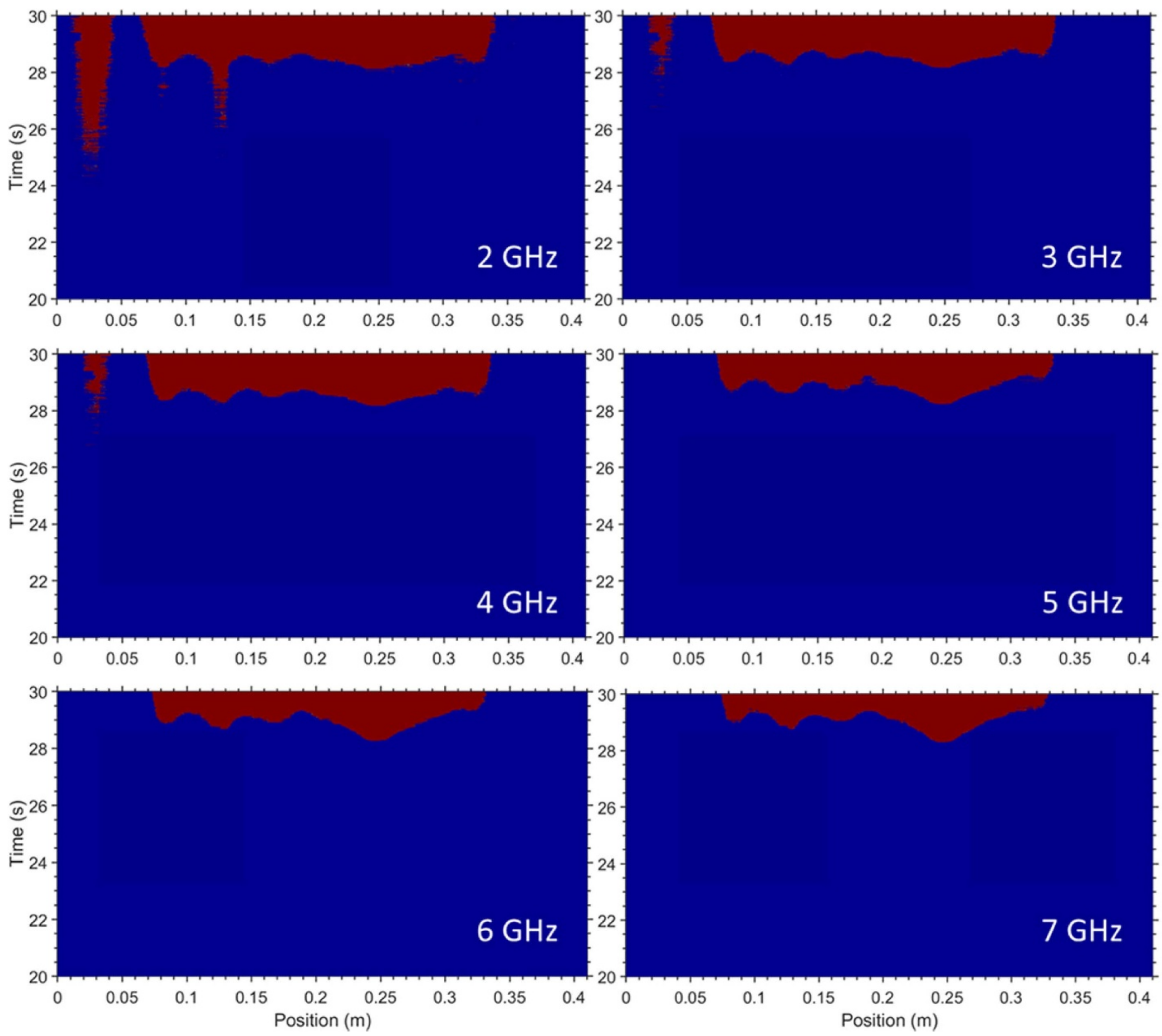

Figure 16. Series of spectral shift maps generated from the same dataset of figure 14, each with a different spectral shift threshold that defines two regions and a border between them. The red regions have a spectral shift higher than the threshold, whereas the blue regions have a spectral shift lower than the threshold.

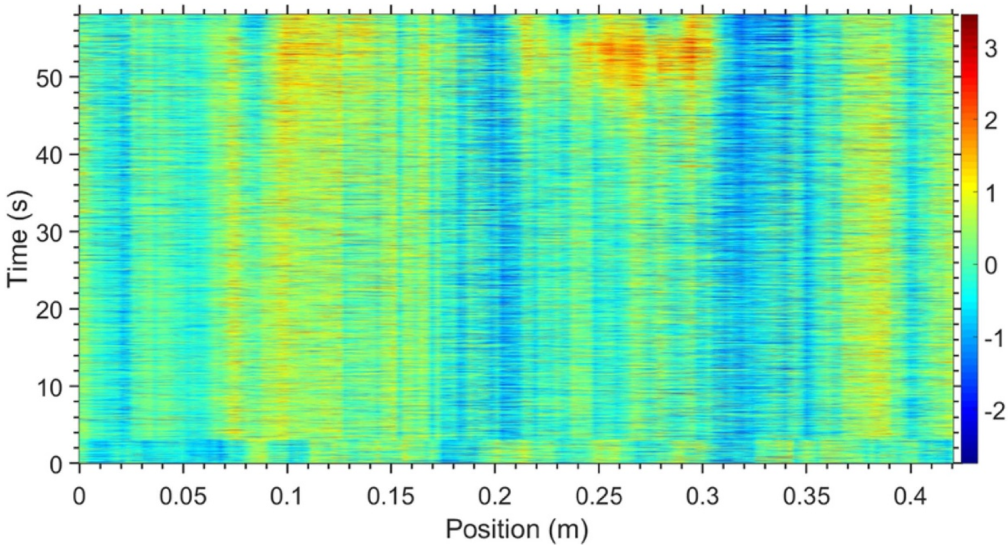

Figure 17. Spectral Shift map of current ramp with cable bent to a radius of 55 mm.

before runaway (during the current ramp, see especially the time window from 23 s to 28 s). The unexpected part, however, is that a different spot, at about 0.25 m, shows a much faster increase in Spectral Shift upon runaway, although it was 'healthier' during the current ramp. This suggests that a quench initiation spot is not uniquely defined, since each spot seems to have a distinct evolution.

To further shed light on the behavior, a set of Spectral Shift maps is shown in figure 16, where a Spectral Shift threshold is used to divide the space-time into regions where the Spectral Shift is higher or lower than the threshold. The contour represents the points, in space and time coordinates, that crossed the threshold, i.e. the boundary between the regions. These plots show that if we consider weak normal zones, for example those that create a Spectral Shift of 2 GHz, then it would appear that the 'stable' hot spot at 0.125 m is the initiation spot. If we consider stronger normal zones, however, for example 6 or 7 GHz, the initiation point would be at 0.25 m. This is because the 'stable' hot spots evidenced during the current ramp (e.g. 0.13 m), although they are the first ones to appear, run away at a lower rate than spots that were colder during the ramp (e.g. the spot at 0.25 m, which is colder during the ramp, but runs away at a much faster rate). The maps in figure 16 provide another point of view of the same finding that can be appreciated from the functions of time in figure 15.

3.3. Quench experiments performed using two large current adapters

Another experimental setup has been used for experiments consisting of the same cable bent at a radius of 55 mm, after undergoing bend tests. Results and detailed analysis of the bending experiments can be found in [44]. In this case, the larger, cylindrical, copper adapters are used for current connections at both ends (see figure 3). The same experiments shown so far have been performed again with the large current adapters. Figure 17 shows the Spectral Shift map of the current ramp. The limits on the color bar are kept the same as the color map shown previously. With this new setup, the 'stable' hotspots that were generated previously are now absent, as can be seen in figure 17. However, a small Spectral Shift build up remains around the 0.25–0.27 m region. These results indicate that the hotspots were primarily related to the limited current redistribution due to the use of small current leads.

A quench run with the same conditions and procedure parameters as shown in figure 5 was carried out with the larger current adapters; the results are included in figure 18 as a Spectral Shift map. Note that the absence of 'stable' hotspots initiated during the ramp made the propagation front smoother compared to the equivalent run with the smaller current adapters (figure 5), with the exception of a relatively small 'secondary' hot spot at about 0.125 m.

The results of an 'overcurrent' with setup comprising bent cable and large current leads are shown in figure 19. With this setup, as evidenced already by the quench experiment, the 'stable' hotspots are almost completely absent, and therefore the only initiation point remains at about 0.255 m. Because of its twist pitch, the fiber follows a helical path along the wire length. Thus, a smooth, straight propagation front is associated with a thermal transient of cylindrical symmetry propagating at constant speed. In the overcurrent experiment, however, the propagation front shows 'fringes' superimposed to a smooth, straight line propagation. This is a strong indication that the normal zone is initiated and propagates in a non-cylindrical symmetry. The propagation initiated by the heater (figure 18) shows the normal zone propagating in cylindrical symmetry, consistent with the fact that the heater is practically a cylinder that surrounds the cable, 1 cm in length. The propagation initiated by the overcurrent (figure 19) shows fringes in the propagation front, superimposed to straight lines. The periodic, quasi-sinusoidal fringe associated with the propagation front suggests that the normal zone does not initiate in cylindrical symmetry, consistent with the fact that, without

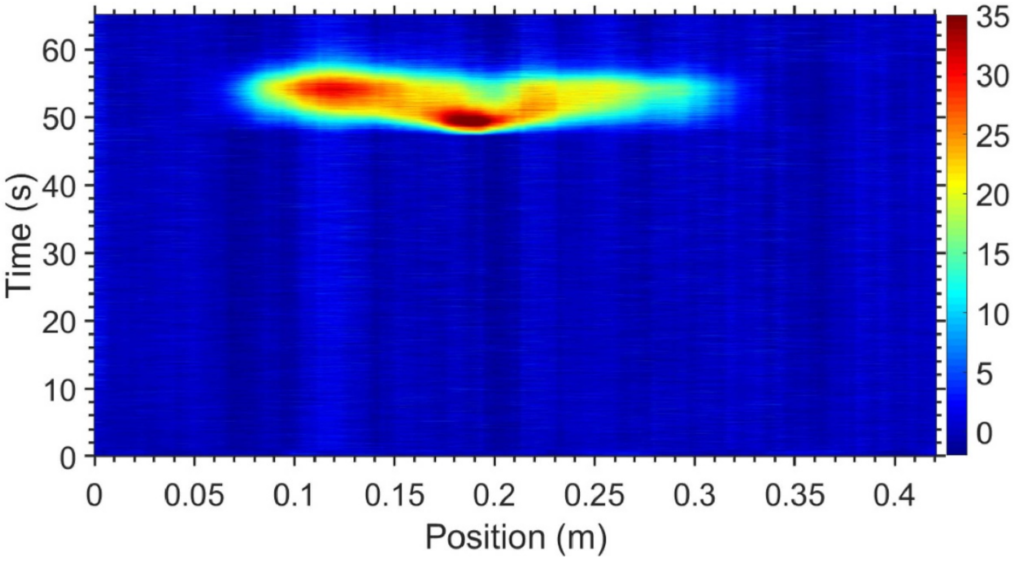

Figure 18. Spectral Shift map of quench induced by a heater with cable bent to a radius of 55 mm.

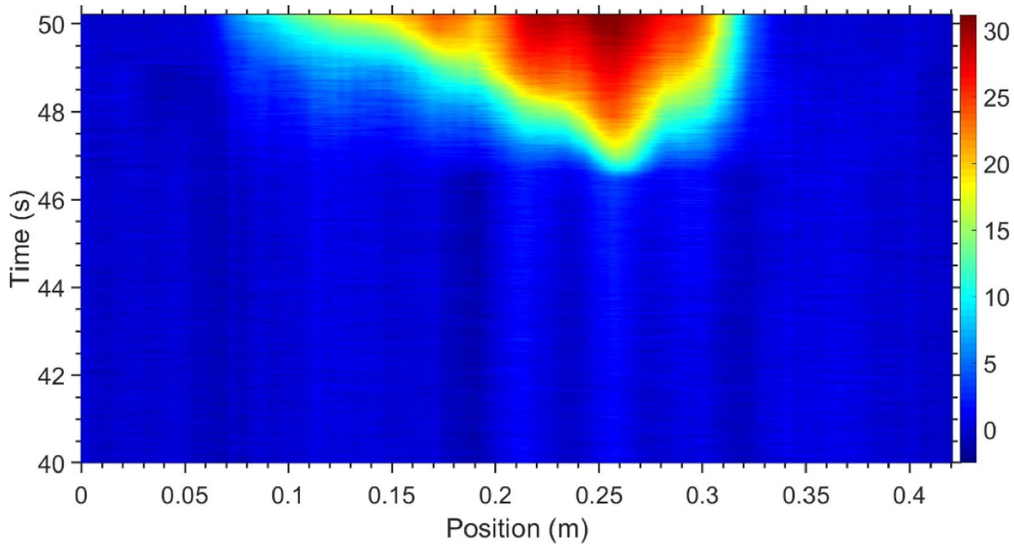

Figure 19. Spectral Shift map of quench induced by an overcurrent with cable bent to a radius of 55 mm.

the aid of a heater, the initiation spot will not have cylindrical symmetry.

3.4. Estimation of normal zone propagation velocity

The NZPV can be extracted from the results of quench and overcurrent measurements. Due to the very high spatial resolution of the RIOF technique, the NZPV can be accurately calculated as a function of time during propagation. The approach used, which is not possible with voltage taps, is based on the Spectral Shift data as a function of position and time. A propagation front is defined, using a Spectral Shift criterion of 5 GHz; the position of the boundary of the normal region is then mapped as a function of time. The derivative of the boundary position with respect to time is, by definition, the normal zone propagation velocity.

The NZPV as a function of time is estimated for a quench experiment, with a normal zone initiated by the heat pulse, and an overcurrent experiment, where the normal zone is initiated by heating in the superconducting tapes. The position of the propagation front versus time for the quench case is shown in figure 20. The position has been determined and plotted with 200 ms time intervals. Note that the experimental data points are not well fitted with a linear function over the entire time interval. Initially, the slope is lower to then increase and settle to a fairly constant speed. Since the NZPV is not constant throughout the propagation, two regions are identified and fitted separately. The slope of the first time region, from 47.4 s to 47.8 s, is calculated to be 2.5 cm s^{-1}, whereas the second region shows an NZPV of 6.2 cm s^{-1}, measured along the length of the fiber.

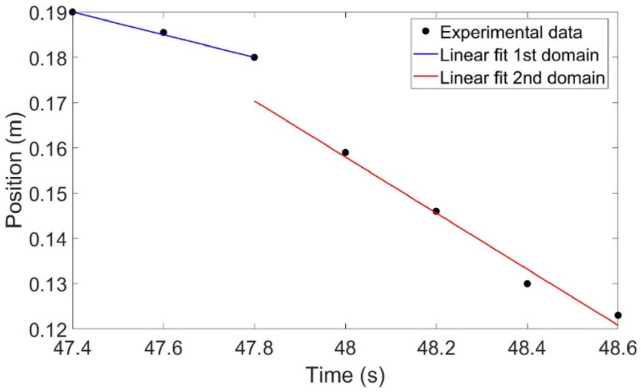

Figure 20. Position of the normal zone propagation front as a function of time for the quench case. The time derivative of the position versus time is the normal zone propagation velocity. The domain is divided into two linear time regions, indicated with linear fits.

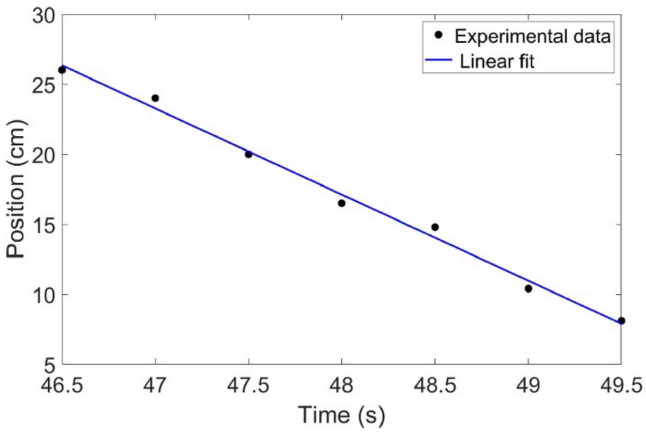

Figure 21. Position of the normal zone propagation front as a function of time for the overcurrent case. Unlike the quench case, only one regime can be identified here, with a constant propagation velocity. The slope of the line is the normal zone propagation velocity.

Using the same approach, the position of the propagation front for the overcurrent case is plotted as a function of time and can be seen in figure 21, from the beginning of the propagation. In this case, the propagation velocity is fairly constant throughout and does not show two different time windows with different speeds. The graph in figure 21 includes a linear fit of the experimental points and shows that the NZPV is about 6.1 cm s^{-1}, also defined along the length of the fiber. Because the fiber is wound at a pitch of about 38 mm at a radius of only 1.24 mm, the fiber is about 2% longer than the sample. The NZPV measured along the length of the sample is thus about 98% of the NZPV measured along the fiber.

The two regimes with two different NZPV showed by the quench initiated by the heater, compared to the unique regime showed by the overcurrent case, suggest that the mechanism that initiates the transition is responsible for the propagation behavior. In fact, in the first case, the material transitions because of an increase in temperature, as opposed to an increase in current density. An increase in temperature will have to exceed the current sharing temperature of each tape to cause the maximum resistive heating that drives the propagation. This could explain the slow initial propagation of the quench induced by the heater.

4. Conclusion

A SMART CORC® wire has been designed and manufactured by integrating optical fibers into groves extruded into the copper core. The optical fiber showed its ability to detect and locate the development of local hotspots induced by overcurrent or when a heater induced a local hotspot. The importance of cable terminations and the adapters to inject current into the terminations in preventing hot spots has been highlighted via the use of different terminal adapter configurations. Local heating was within the terminations and in the CORC® wire near one of the terminations could clearly be measured with the fiber when small current adapters that were inadequate to inject current evenly into each tape were used.

The normal zone propagation velocity has been calculated using experimental Spectral Shift data when a heat pulse initiated a quench and when the quench was initiated by overcurrent. The NZPV measured during the heater induced transient was about 2.5 cm s^{-1} over the first 500 ms and then increased to 6.2 cm s^{-1} as all the tapes became normal. The NZPV was measured to be 6.1 cm s^{-1} for the normal zone driven by an overcurrent.

Integrated optical fibers in multi-tape HTS cables that allow operation to within the current sharing regime, such as CORC® wires, are a valuable tool to determine possible origins of local dissipation during normal operation and when driven into a dissipative mode where significant heating occurs. The method allows for monitoring of the operating state of the conductor, but also allows improvements that result in a minimization of resistive loss in the cable system.

Acknowledgments

This work was supported by the United States Department of Energy, Office of Science, under (Grant Nos. DE-SC0014009 and DE-SC0018706).

ORCID iDs

F Scurti https://orcid.org/0000-0002-4814-165X
J D Weiss https://orcid.org/0000-0003-0026-3049
D C van der Laan https://orcid.org/0000-0001-5889-3751

References

[1] Mangiarotti F J and Minervini J V 2015 Advances on the design of demountable toroidal field coils with REBCO superconductors for an ARIES-I class fusion reactor *IEEE Trans. Appl. Supercond.* **25** 1–5

[2] van Nugteren J, Kirby G, Murtomaki J, DeRijk G, Rossi L and Stenvall A 2018 Toward REBCO 20 T+ dipoles for accelerators *IEEE Trans. Appl. Supercond.* **28** 1–9

[3] Badel A *et al* 2016 Advances in the development of a 10-kA class REBCO cable for the EuCARD2 demonstrator magnet *IEEE Trans. Appl. Supercond.* **26** 1–8

[4] Trociewitz U P, Dalban-Canassy M, Hannion M, Hilton D K, Jaroszynski J, Noyes P, Viouchkov Y, Weijers H W and Larbalestier D C 2011 35.4 T field generated using a layer-wound superconducting coil made of (RE)$Ba_2Cu_3O_{7-x}$ (RE = rare earth) coated conductor *Appl. Phys. Lett.* **99** 3

[5] Fujiwara N, Hayashi H, Nagaya S and Shiohara Y 2010 Development of YBCO power devices in Japan *Physica* C **470** 980–5

[6] Rupich M W 2015 Second-generation (2G) coated high-temperature superconducting cables and wires for power grid applications *Supercond. Power Grid* (Cambridge: Woodhead Publishing) pp 97–130

[7] Zhang Y, Lehner T F, Fukushima T, Sakamoto H and Hazelton D W 2014 Progress in production and performance of second generation (2G) HTS wire for practical applications *IEEE Trans. Appl. Supercond.* **24** 1–5

[8] Fietz W H, Wolf M J, Preuss A, Heller R and Weiss K-P 2016 High-current HTS cables: status and actual development *IEEE Trans. Appl. Supercond.* **26** 1–5

[9] Takayasu M, Chiesa L, Allen N C and Minervini J V 2016 Present status and recent developments of the twisted stacked-tape cable conductor *IEEE Trans. Appl. Supercond.* **26** 25–34

[10] Barth C 2013 *High Temperature Superconductor Cable Concepts for Fusion Magnets* (Karlsruhe: KIT Scientific Publishing) 254

[11] Glasson N, Staines M, Allpress N, Pannu M, Tanchon J, Pardo E, Badcock R and Buckley R 2017 Test results and conclusions from a 1 MVA superconducting transformer featuring 2G HTS Roebel cable *IEEE Trans. Appl. Supercond.* **27** 1–5

[12] Fetisov S S *et al* 2016 Development and characterization of a 2G HTS Roebel cable for aircraft power systems *IEEE Trans. Appl. Supercond.* **26** 1–4

[13] van der Laan D C, Weiss J D, Noyes P, Trociewitz U P, Godeke A, Abraimov D and Larbalestier D C 2016 Record current density of 344 A mm^{-2} at 4.2 K and 17 T in CORC® accelerator magnet cables *Supercond. Sci. Technol.* **29** 055009

[14] Majoros M, Sumption M D, Collings E W and van der Laan D 2016 Stability and normal zone propagation in YBCO CORC cables *Supercond. Sci. Technol.* **29** 044006

[15] van der Laan D C, Weiss J D and McRae D M 2019 Status of CORC® cables and wires for use in high-field magnets and power systems a decade after their introduction *Supercond. Sci. Technol.* **32** 033001

[16] Weijers H W, Trociewitz U P, Marken K, Meinesz M, Miao H and Schwartz J 2004 The generation of 25.05 T using a 5.11 T Bi2Sr2CaCu2Ox superconducting insert magnet *Supercond. Sci. Technol.* **17** 636–44

[17] Takayasu M, Chiesa L, Noyes P D and Minervini J V 2017 Investigation of HTS twisted stacked-tape cable (TSTC) conductor for high-field, high-current fusion magnets *IEEE Trans. Appl. Supercond.* **27** 1–5

[18] Whyte D G, Minervini J, LaBombard B, Marmar E, Bromberg L and Greenwald M 2016 Smaller & sooner: exploiting high magnetic fields from new superconductors for a more attractive fusion energy development path *J. Fusion Energy* **35** 41–53

[19] Wolf M J, Fietz W H, Bayer C M, Schlachter S I, Heller R and Weiss K-P 2016 HTS CroCo: a stacked HTS conductor optimized for high currents and long-length production *IEEE Trans. Appl. Supercond.* **26** 19–24

[20] Goldacker W, Grilli F, Pardo E, Kario A, Schlachter S I and Vojenčiak M 2014 Roebel cables from REBCO coated conductors: a one-century-old concept for the superconductivity of the future *Supercond. Sci. Technol.* **27** 093001

[21] Himbele J J, Badel A and Tixador P 2016 HTS dipole magnet for a particle accelerator using a twisted stacked cable *IEEE Trans. Appl. Supercond.* **26** 1–5

[22] Bykovsky N, Uglietti D, Wesche R and Bruzzone P 2016 Design optimization of round strands made by twisted stacks of HTS tapes *IEEE Trans. Appl. Supercond.* **26** 1–7

[23] van der Laan D C, Goodrich L F, Noyes P, Trociewitz U P, Godeke A, Abraimov D, Francis A and Larbalestier D C 2015 *Engineering current density in excess of 200 A mm^{-2} at 20 T in CORC® magnet cables containing RE-$Ba_2Cu_3O_{7-\delta}$* tapes with 38 μm thick substrates *Supercond. Sci. Technol.* **28** 124001

[24] van der Laan D C, Noyes P D, Miller G E, Weijers H W and Willering G P 2013 Characterization of a high-temperature superconducting conductor on round core cables in magnetic fields up to 20 T *Supercond. Sci. Technol.* **26** 045005

[25] Weiss J D, Mulder T, Ten Kate H J and van der Laan D C 2017 Introduction of CORC® wires: highly flexible, round high-temperature superconducting wires for magnet and power transmission applications *Supercond. Sci. Technol.* **30** 014002

[26] Weiss J D, van der Laan D C, Hazelton D, Knoll A, Carota G, Abraimov D, Francis A, Small M A, Bradford G and Jaroszynski J 2020 Introduction of the next generation of CORC® wires with engineering current density exceeding 650 A mm^{-2} at 12 T based on superpower's ReBCO tapes containing substrates of 25 μm thickness *Supercond. Sci. Technol.* **33** 44001

[27] Wang X, Dietderich D R, DiMarco J, Ghiorso W B, Gourlay S A, Higley H C, Lin A, Prestemon S O, Laan D V D and Weiss J D 2019 A 1.2 T canted cosθ dipole magnet using high-temperature superconducting CORC® wires *Supercond. Sci. Technol.* **32** 75002

[28] Van Der Laan D C *et al* 2020 A CORC® cable insert solenoid: the first high-temperature superconducting insert magnet tested at currents exceeding 4 kA in 14 T background magnetic field *Supercond. Sci. Technol.* **33** 05LT03

[29] Wang X *et al* 2020 Development and performance of a 2.9 Tesla dipole magnet using high-temperature superconducting CORC® wires *Supercond. Sci. Technol.* **34** 015012

[30] Ye L, Cruciani D, Effio T, Hunte F and Schwartz J 2013 On the causes of degradation in round wires and coils by quenching at 4.2 K *IEEE Trans. Appl. Supercond.* **23** 6400811

[31] Song H, Gagnon K and Schwartz J 2010 Quench behavior of conduction-cooled $YBa_2Cu_3O_7$-delta coated conductor pancake coils stabilized with brass or copper *Supercond. Sci. Technol.* **23** 109802

[32] Wang X, Trociewitz U P and Schwartz J 2007 Near-adiabatic quench experiments on short $YBa_2Cu_3O_7$-delta coated conductors *J. Appl. Phys.* **101** 053904

[33] Trillaud F, Chea Ang I, Kim W-S, Lee H G, Iwasa Y and Voccio J P 2007 Protection and quench detection of YBCO coils results with small test coil assemblies *IEEE Trans. Appl. Supercond.* **17** 2450–3

[34] Wang X, Trociewitz U P and Schwartz J 2009 Self-field quench behaviour of $YBa_2Cu_3O_7$-delta coated conductors with different stabilizers *Supercond. Sci. Technol.* **22** 13

[35] Wang X, Trociewitz U P and Schwartz J 2011 Critical current degradation of short $YBa_2Cu_3O_7$-delta coated conductor due to an unprotected quench *Supercond. Sci. Technol.* **24** 035006

[36] Song H and Schwartz J 2009 Stability and quench behavior of $YBa_2Cu_3O_{7-x}$ coated conductor at 4.2 K, self-field *IEEE Trans. Appl. Supercond.* **19** 3735–43
[37] Schwartz J 2014 Quench in high temperature superconductor magnets *Proc. of WAMSDO: Workshop on Accelerator Magnet Superconductors, Design and Optimization CERN* (*Geneva, Switzerland*, *21-29 2013*) (https://doi.org/10.5170/CERN–2013–006)
[38] Froggatt M and Moore J 1998 High-spatial-resolution distributed strain measurement in optical fiber with Rayleigh scatter *Appl. Opt.* **37** 1735–40
[39] Gifford D K *et al* 2007 Swept-wavelength interferometric interrogation of fiber Rayleigh scatter for distributed sensing applications *Proc. SPIE* pp 67700F
[40] Scurti F, Ishmael S, Flanagan G and Schwartz J 2016 Quench detection for high temperature superconductor magnets: a novel technique based on Rayleigh-backscattering interrogated optical fibers *Supercond. Sci. Technol.* **29** 03LT01
[41] Scurti F and Schwartz J 2017 Optical fiber distributed sensing for high temperature superconductor magnets *Proc. SPIE—Int. Soc. Opt. Eng.* **10323** 103238Q
[42] Scurti F, Sathyamurthy S, Rupich M and Schwartz J 2017 Self-monitoring 'SMART' (RE)$Ba_2Cu_3O_{7-x}$conductor via integrated optical fibers *Supercond. Sci. Technol.* **30** 114002
[43] Scurti F, Mcgarrahan J and Schwartz J 2017 Effects of metallic coatings on the thermal sensitivity of optical fiber sensors at cryogenic temperatures *Opt. Mater. Express* **7** 1754-66
[44] Van Der Laan D C, Weiss J D, Scurti F and Schwartz J 2020 CORC®wires containing integrated optical fibers for temperature and strain monitoring and voltage wires for reliable quench detection *Supercond. Sci. Technol.* **33** 085010